Analyst

Accepted Manuscript

ROYAL SOCIETY OF CHEMISTRY

www.rsc.org/analyst

Wide-Field Raman Imaging of Dental Lesions

Shan Yang[1], Bolan Li[1], Anna Akkus[2], Ozan Akkus[1,3,4,*], Lisa Lang[2]

1. Department of Mechanical and Aerospace Engineering, Case Western Reserve University, Cleveland, OH, 44106, USA
2. School of Dental Medicine, Case Western Reserve University, Cleveland, OH, 44106, USA
3. Department of Orthopaedics, School of Medicine, Case Western Reserve University, Cleveland, OH, 44106, USA
4. Department of Biomedical Engineering, Case Western Reserve University, Cleveland, OH, 44106, USA

[*] Corresponding author: Ozan. Akkus@case.edu

Abstract

Detection of dental caries at the onset remains as a great challenge in dentistry. Raman spectroscopy could be successfully applied towards detecting caries since it is sensitive to the amount of the Raman active mineral crystals, the most abundant component of enamel. Effective diagnosis requires full examination of a tooth surface via a Raman mapping. Point-scan Raman mapping is not clinically relevant (feasible) due to lengthy data acquisition time. In this work, a wide-field Raman imaging system was assembled based on a high-sensitivity 2D CCD camera for imaging the mineralization status of teeth with lesions. Wide-field images indicated some lesions to be hypomineralized and others to be hypermineralized. The observations of wide-field Raman imaging were in agreement with point-scan Raman mapping. Therefore, sound enamel and lesions can be discriminated by Raman imaging of the mineral content. In conclusion, wide-field Raman imaging is a potentially useful tool for visualization of dental lesions in the clinic.

1. Introduction

Dental caries is the most significant problem in the oral health world-wide. Caries is affecting vast majority of adults and over 60% of school-age children in industrialized counties [1], with a quarter of Americans losing all their teeth by 65 years old [2]. Caries involves gradual demineralization of the enamel layer by bacterial activity. When left undetected, caries invades dentin and may lead to a root channel treatment. Late stage carious lesions are repaired by restoration using various dental materials; however, over the lifetime of the individual, the restoration may fail due to recurrent caries and more costly interventions such as a crown, fixed dental prosthesis, or dental implants may be needed. If caries formation is detected early, it is possible to remineralize the lesion [3, 4] and avoid the catastrophic cascade of degradation that results in the loss of the tooth. Unfortunately, early onset lesions elude clinically available tools such as visual-tactile observation and x-ray imaging [5, 6]. Existing modalities (quantitative fluorescence, electrical conductance and as such) are reported to have high false positive rates or high false negative rates in detecting the early onset caries [7]. Therefore, there is an acute need for new technologies that will provide both high sensitivity (probability of diagnosing caries in patients with caries) and high specificity (probability of excluding caries in patients without caries).

Visualization of the mineralization status of enamel would be invaluable for early detection because caries are associated with changes in the mineralization of tooth [8]. The phosphate group in the mineral component of enamel scatters the Raman signal strongly. As a result, Raman spectroscopy has long been a powerful tool for assessing mineral content in dental and other mineralized tissues such as bone [9-12]. However, existing Raman modalities depend on

the inspection of the suspected locations by fiber optic probes manually [12] which is not conducive to systematic coverage of the oral space in a clinically feasible time frame. The inability to generate images of the mineralization of the complete surface of a tooth is a barrier to translation of Raman based techniques into clinic.

In classical Raman imaging, laser light is translated point by point (or as a line) over the sample space and an array of spectra are recorded during the process. Therefore, spatial scans require moving the sample with respect to the laser (or vice versa), which takes a long duration, and limits clinical applicability. Wide-field Raman imaging, or global Raman imaging, system captures 2D image of select wavenumber of interest using spectral filters and 2D-CCD cameras. Wide-field Raman images of carbon nanotubes and Si/Ti structured wafer have been reported using green or red laser [13, 14]. In this work, we integrated a wide-field Raman imaging system capable of acquiring images over the full field of view (FOV) based on near-infrared (NIR) laser at 785 nm, NIR optimized 2D-CCD camera, and a cost-effective dielectric filter. The results demonstrated that variation of mineralization between sound enamel and lesions can be imaged in a wide-field context by using the phosphate band at 960 cm^{-1} only. The capability to image mineral distribution over larger fields of views in a shorter time would enhance the translational prospect of Raman for detecting dental caries and for surveying the success of remineralization treatments.

2. Materials and Methods

Alligator and human teeth were used in this study. Human teeth were collected under the approvals of Institutional Review Boards of Case Western Reserve University (IRB# EM-13-17).

The alligator tooth demonstrates a stepwise increase of mineralization at the dentin-enamel junction; therefore, it was used to test whether the wide-field Raman imaging set up can detect mineralization changes. Alligator tooth was sliced perpendicular to its longer axis to expose the dentinoenamel junction using a precision low-speed diamond blade saw (ISOMET 1000). Human teeth were extracted from patients as part of the regular clinical treatment. Two teeth demonstrating identifiable lesions were examined in this study. A wide-field Raman imaging system was custom-integrated in our lab to record global Raman images of specimens. Images were taken at the lesion locations, the sound enamel as well as transitional regions between enamel and caries.

The schematic diagram of the wide-field Raman imaging system is illustrated in Fig. 1a. The excitation source was a single mode wavelength stabilized 785 nm laser (I0785S50100B, Innovative Photonic Solutions, NJ) with 100 mW output. The beam diameter at which the intensity decreases to $1/e^2$ of its peak intensity is 0.5 mm. A long pass dichroic beam splitter (FF801-Di02-25x36, Semrock, NY) was used to deliver the laser light though the low magnification objective lens (f = 25 mm, AC127-025-B, Thorlabs, NJ) to the sample, while allowing the Raman signal to be collected in the backscattering regime simultaneously. A negative cylindrical lens (f = – 200 mm) was used to defocalize the laser spot on the sample into an ellipsoidal profile. The cylindrical lens was removed from the optical path to collect the information over a round spot as well. Enamel is 92-96% mineral [15] and the 960 cm^{-1} peak of phosphate symmetric stretch band is sufficient for obtaining the amount of mineralization. A narrow band pass filter (LL01-852-25, Semrock, NY) with 3 nm bandwidth at FWHM was used to select the 960 cm^{-1} mineral Raman signals, and a pair of edge filters (LP02-808RU, Semrock,

NY, USA) with OD 7 at 785 nm was used to further suppress the residual excitation laser light. The wide-field Raman image was amplified by an anti-reflection coated lens (f = 200 mm) before it was captured by the CCD camera (Ikon M 934, Andor, CT) equipped with a back illuminated sensor optimized for near infrared detection (90% quantum efficiency at 850 nm). The CCD camera has a resolution of 1024 × 1024 sensor with pixel dimensions of 13 × 13 μm^2. An OEM-Raman system (785L, Wasatch Photonics, NC) was used to observe the Raman spectrum picked up by the flip beam splitter (BSN11, Thorlabs, NJ), which was flipped off the optical path during image acquisition.

The narrow band pass filter is continuously tunable from 823 to 852 nm, corresponding to 600 to 1001 cm^{-1} Raman shift at 785 nm excitation. At 9 degrees incidence angle, the center wavelength was tuned to 960 cm^{-1} Raman shift to allow transmitting the mineral Raman signal, as shown in Fig. 1b (blue-solid curve), while blocking the photons at other Raman shifts. The wide-field Raman image acquired with such a configuration, however, included both the mineral Raman signal and the background-florescence in range. By rotating the band pass filter to near 17 degrees of incidence angle, only the auto-fluorescence band centered at ~880 cm^{-1} were allowed to be transmitted, as shown in Fig. 1b (red-dashed curve). A second wide-field Raman image acquired in this configuration was used to correct the background fluorescence contribution by subtracting it from the first wide-field Raman image. Appropriate time of photobleaching was applied to the extent that the background fluorescence did not have measurable change in the time length of each test.

The results acquired from the wide-field system were compared with images obtained by point-by-point Raman scans of similar regions using a research grade Raman microscope (Xplora, Horiba Jobin Yvon), also at 785 nm excitation. Raman maps were collected from the tooth samples using an X10 objective (Olympus) at 25μm scan step size along both directions. The microscope was equipped with a computer controlled 3-axes stage which allows positioning the laser on the sample. Each spectrum was obtained as the average of 5 consecutive spectra each collected for 1 second. The raw data resulting from the mapping procedure were exported to MATLAB and the fluorescence background correction was performed by subtracting the valley intensity at 1000 cm^{-1} from the peak intensity at 960 cm^{-1} of the raw mineral Raman signal. The chemical image was constructed based on the intensity of the characteristic 960 cm^{-1} peak of mineral signal obtained from background corrected spectra.

A transversely sectioned and polished alligator tooth was mounted on an aluminum stub and coated with a thin carbon coating. The sample was characterized using an FEI Helios 650 scanning electron microscope. The imaging of the enamel-dentin interface was performed in back scattered mode using a solid state retractable detector. In this mode the contrast is highly sensitive to the atomic weight and density. Since calcium is the major component with the highest atomic number, regions with greater levels of mineralization result in a high backscattered electron yield and therefore appear brighter in the ensuing SEM image.

3. Results:

The mineralization scores of the wide-field Raman images at the dentinoenamel junction of alligator was greater for the enamel region at 960 cm^{-1} than the dentin region (Fig. 2c). The image acquired at 880 cm^{-1} wavenumber did not differ between the enamel and the dentin

implying comparable background fluorescence at the two locations. Subtraction of the 880 cm^{-1} image from the 960 cm^{-1} image resulted in the background fluorescence corrected image in Fig. 2e. The wide-field image was over an ellipsoidal region (100 µm by 250 µm) due to the insertion of the cylindrical lens on the excitation path. As expected, the corrected Raman image demonstrated a stepwise increase of mineral content at the junction between the enamel (higher mineralization) and the dentin (lower mineralization) regions (Fig. 2e). This observations was confirmed by the backscattered electrons images where enamel was white and the dentin region was gray, indicating a greater amount of calcium in the enamel reflect greater number of electrons than dentin (Fig. 2b).

The Raman point-by-point map (Fig. 3a) obtained by the commercial Raman system from the same area (dashed red block in Fig. 2a) confirmed higher mineral concentration in enamel as that in fluorescence corrected wide-field Raman image (Fig. 3b), which was normalized by its own maximum from Fig. 2d for better comparison with the point Raman map. Ten points were selected from dentin and enamel regions (Fig.3c) to obtain average mineralization values for global and point maps. The mineralization scores of enamel obtained by point maps indicated a greater mineralization score than that obtained by global imaging (Fig. 3d). The p-values for student's t-test were 0.000 and 0.006 for mapping and global imaging, respectively. The total scan time for point maps was 52 minutes using the step size and signal acquisition times mentioned in the methods section. Both the 880 cm^{-1} and 960 cm^{-1} global images were acquired in 2 minutes with ~50 mW 785 nm laser delivered on the sample.

The same background correction procedure described in Fig. 2 was performed over a human tooth with a white lesion. A fluorescence background corrected wide-field Raman image (Fig. 4d) taken from the transition area (Fig. 4a) between sound enamel (lower half) and white lesion (upper half) indicated that the mineral Raman signal decreased gradually from sound enamel to lesion area. The wide-field image based on background fluorescence intensity at near 880 cm^{-1} indicated higher fluorescence level for the lesion (Fig. 4c).

Typical wide-field Raman images from the central areas of sound enamel and lesion of a human tooth are shown in Figs. 5d and 5e, respectively. A point-by-point Raman map of enamel and lesion (Fig 5a) confirmed that the lesion was hypomineralized relative to the sound enamel (Figs. 5b and 5c). In agreement with the point map, the mineralization observed by wide-field images was greater in the sound enamel (Fig. 5d) than the lesion (Fig 5e). Ten random points were selected in each imaging area and the average mineral Raman signal at 960 cm^{-1} were comparable between point maps and global images (Fig. 5f).

A lesion on another tooth (Fig. 6a) demonstrated that the lesion was hypermineralized in comparison to the sound enamel surrounding the lesion as confirmed by point-by-point Raman map (Figs. 6b and 6c). Wide-field observations agreed with point Raman map where the lesion (Fig. 6e) was more mineralized than the sound enamel (Fig. 6d). Representative Raman spectra from central sound enamel region and lesion from both hypo and hyper mineralized lesions (Figs. 5g and 6f) indicated that in addition to the intensity change related to mineral concentration, additional Raman peaks associated with the organic phase were observed in the hypomineralized lesion.

A wide-field image covering a larger area was successfully acquired by using lower magnification lens as shown in Fig 7. Lenses with focal length of 25 mm and 50 mm were used for acquiring the wide-field images from the same tooth at the similar area (Figs. 7a and 7b). The full FOV provided by these lenses had diameters of ~1 mm and 2.5 mm, respectively. However, the effective areas which yielded Raman images were about ~100 × 250 μm^2 (Fig. 7a) with 25 mm lens in contrast to ~200 ×600 μm^2 (Fig. 7b) with 50 mm lens. The limitations in the area coverage of Raman information is mainly due to the reduction in the intensity of laser illumination with increasing distance from the center of the FOV.

Time-dependent Raman spectra of bovine bone acquired by the 785 nm and 1064 nm indicated fluorescence background decreased with the photobleaching (Fig. 9). The 785 nm set of data were taken with 50 mW laser power and the exposure time was 1 seconds. The data were averaged 10 times. The 1064 nm set of data were taken with 250 mW and the exposure time was 10 seconds. The fluorescence intensity decreased exponentially (data not shown) and reached steady level after ~15 minutes photobleaching with 785 nm excitation. The fluorescence level of the 1064 nm excitation is over an order of magnitude less than that of 785 nm and photobleaching is not effective in its reduction.

4. Discussion

Major wide-field Raman imaging related reports in literature to date are generally associated with active Raman agents such as graphene/carbon nanotubes [13, 14], and pharmaceutical drugs [16, 17]. A recent wide-field Raman imaging study collected images from surface enhanced Raman scattering (SERS) agents implanted in mice [18]. Wide-field Raman imaging has not been reported in the literature to address the dental caries. We demonstrated that the wider-field

direct Raman imaging of dental caries is feasible by using a combination of high-performance optical filters, ultra-sensitive, low noise CCD detectors and a background fluorescence correction algorithm.

Carbonated apatite crystals are the most abundant component of both enamel (90% by volume) [19] and dentin (48% by volume) [20] in human teeth. Dentin contains 25% organic matrix and 25% water by volume, while enamel contains less organic matrix and very small amount of water. The ratio of the mineral signal intensity is approximately 1.7 to 1 (enamel:dentin) on two sides (Fig. 3c) when assessed by the global Raman images. The Raman mapping obtained by the commercial Raman microscope had a higher ratio of about 3.5 to 1. While both methods agreed in terms of presenting greater mineralization scores for enamel than dentin, the magnitude of the variation differed. One reason could be the confocal hole in the commercial Raman system may have limited the collection of Raman signals from a small volume. In the case of global imaging, the laser was illuminating a much larger volume and the diffusive exchange of Raman signals may have contributed to the difference. The mineralization of the enamel and the lesion obtained by the two methods agreed with each other (Fig.5).

Oral bacteria produce large amount of lactic acid by metabolization of sugars and starch which in turn causes local demineralization. Dental caries initiates when the demineralization process overcomes the physiological remineralization by saliva or clinical repair with fluoride. Early-stage dental remineralization may appear in the form of white lesion on the surface of teeth. However, often the localized mineralization is not detectable to the naked eye or to dental instruments due to limited depth (~50 μm). Therefore, lesions are hard to visually discriminate

from intact enamel. The mineral concentrations of lesions are normally lower than the surrounding sound enamel; such lesions are called hypomineralization lesions. Due to the reduced amount of mineral crystals and increased deposition of organic matrix as well as organic byproducts of bacteria activity, lesions present a lower mineral Raman signal (Fig. 4d, Fig. 5) and higher fluorescence background (Fig. 4c) than sound enamel.

Remineralization and demineralization are two processes that are simultaneously occurring. In some cases the remineralization process exceeds the demineralization after the hypomineralization lesions have formed, a layer of hypermineralized lesion could form on top of the hypomineralized layer. Regardless of the nature of the lesion, hypo or hypermineralized, the global Raman imaging is capable of detecting inherent differences in mineralization levels and the qualitative discrimination is in agreement with the point Raman maps. Typical Raman spectra from the sound enamel and the lesion of the hypomineralized tooth indicated a greater reduction of the mineral concentration after demineralization (Fig. 5g); on the contrary, the Raman signal of mineral crystals in hypermineralized lesion is more intense than that of the sound enamel (Fig. 6f). In addition to the mineral concentration variation, additional Raman peaks were observed from hypomineralized lesion. Those peaks probably were associated with the organic byproducts formed during the bacterial invasion; additional studies are needed to fully understand their nature.

The collection time of a Raman image taken with f = 25 mm lens (Figs. 3b or 7a) is 2 minutes. The time for obtaining a point-by-point Raman mapping (Fig. 3a) covering the similar area is ~13 times longer (52 minutes). It is worth to note that this ratio could be higher for imaging larger areas. The area of wide-field imaging is determined by the size of the full FOV covered by

the collecting lens. The collection time for wide-field Raman imaging using different lens thus remain the same if the intensity of the illumination does not change, which can be maintained by increasing the laser power. The possible reduction in collection efficiency due to lower numerical aperture of lenses with larger view can also be compensated by higher laser power. The time for point-by-point mapping is proportional to the area because the illuminating laser is focused and sample damage may occur at higher power.

Global Raman imaging covered ~4 times larger area when a loose focusing f = 50 mm lens was used; due to the limited laser power (50 mW), the integration time was doubled to 4 minutes in order to maintain similar image contrast (Fig. 7b). The image area covered with f = 50 mm lens was ~0.2 × 0.6 mm^2, which is near $1/50^{th}$ of the full FOV covered by the lens. Considering only 50 mW laser was delivered to the sample in the experiments, wide-field Raman imaging from the full FOV covered by the lens (2.5 mm in diameter) is feasible provided that appropriately high powered laser (2.5 W) is utilized. Shorter integration time may be employed after systematic investigation and characterization of the threshold laser power for the wide-field imaging. Ideally, the wide-field image would be expected to cover full surface area of a tooth ~ 4×5 mm^2, which is about 220 times larger than the image area shown in Fig. 7b. Taking into the account of the decrease in the numerical aperture of lenses with lower magnification and the curvature of the tooth surface, major advances are required for imaging of whole tooth surface.

The variation of illumination over the sample stems from distortions/aberrations introduced by optical components, and surface curvature of the sample (when present) that introduces variations in depth of focus. These effects can be accounted for by acquisition of an image taken at 880 cm^{-1} as the reference reflecting the laser intensity variation, and then dividing

the reference image (Fig.2d) from the Raman image (Fig. 2e). The corrected image was then normalized by its peak intensity (Fig. 8b). Following such correction, the enamel/dentin contrast increased and mineral concentration was recovered from more than 50% of the imaged area; which was less than 10% of the full FOV before correction (Fig. 8a). The image taken at 880 cm^{-1} was chosen as reference because it was not associated with a Raman peak, therefore, it did not vary with variations in mineral content. However, this correction scheme has room for improvement because the location where the laser has peak intensity had greater mineralization scores than the rest. A reference image of the pure reflection of laser profile (without notch filters in the path) can be used instead as a more accurate and faster way to correct for the variations in the light wave front.

The fluorescence intensity of biological media will decrease exponentially under laser-induced chemical degradation [21]. Excitation with longer wavelength laser produces less fluorescence because the lower photon energy is less effective in driving molecules to excited energy states which lead to fluorescence. In order to minimize the fluorescence intensity difference between the I_{960} spectra and the I_{880} spectra, up to 20 minutes of photobleaching was applied before acquiring the reported global images at 785 nm. Fluorescence background reached the steady state after this period. This prolonged photobleaching duration may be decreased or eliminated by employing longer wavelength excitation, e.g., 1064 nm laser. Considering the power of 1064 nm laser is 5 times higher and it is exposed 10 times longer, the fluorescence comparison between 785 nm and 1064 nm confirmed the dramatic reduction of fluorescence with 1064 nm illumination. The fluorescence background correction may not be needed using 1064 nm excitation because of the minimal fluorescence level and negligible changes under photobleaching (Fig. 9).

5. Conclusion

We demonstrated that wide-field Raman imaging can discriminate sound enamel from lesion in human teeth based on the contrast of the mineral Raman signal distribution. By employing lower magnification lens or additional defocalization of laser beam, larger areas can be covered. On the other hand, attaining full FOV coverage to inspect the surface of an entire tooth remains as a challenge. In summary, wide-field Raman imaging is a promising method in early dental caries detection and can be applied in a fashion to check suspected locations.

Acknowledgements: We thank Dr. Amir Avishai of the Swagelok Center for Surface Analysis at the Case Western Reserve University for assisting with the collection of back scattered electron microscopy image. This study was funded by the research grant R01AR057812 (OA) from the NIAMS institute of NIH. Its contents are solely the responsibility of the authors and do not necessarily represent the official views of the NIH. Special thanks to the Department of Oral and Maxilofacial Surgery of the CWRU School of Dentistry for providing the teeth specimens.

References

1. Petersen, P.E., et al., *The global burden of oral diseases and risks to oral health.* Bulletin of the World Health Organization, 2005. **83**: p. 661-669.
2. *Centers for Disease Control and Prevention [CDC]. Oral Health: Preventing Cavities, Gum Disease,Tooth Loss, and Oral Cancers; 2011. http://www.cdc.gov/chronicdisease/resources/publications/aag/pdf/2011/Oral-Health-AAG-PDF-508.pdf.*
3. ten Cate, J.M., et al., *Elevated Fluoride Products Enhance Remineralization of Advanced Enamel Lesions.* Journal of Dental Research, 2008. **87**(10): p. 943-947.
4. Cochrane, N.J., et al., *New approaches to enhanced remineralization of tooth enamel.* J Dent Res, 2010. **89**(11): p. 1187-97.
5. Ismail, A.I., *Visual and Visuo-tactile Detection of Dental Caries.* Journal of Dental Research, 2004. **83**(suppl 1): p. C56-C66.
6. Zero, D.T., et al., *The Biology, Prevention, Diagnosis and Treatment of Dental Caries: Scientific Advances in the United States.* The Journal of the American Dental Association, 2009. **140**(suppl 1): p. 25S-34S.
7. Amaechi, B.T., *Emerging technologies for diagnosis of dental caries: The road so far.* Journal of Applied Physics, 2009. **105**(10): p. 102047.
8. Arends, J., J. Schuthof, and J.C. Christoffersen, *Inhibition of Enamel Demineralization by Albumin in vitro (Short Communication).* Caries Research, 1986. **20**(4): p. 337-340.

9. Hill, W. and V. Petrou, *Detection of Caries and Composite Resin Restorations by Near-Infrared Raman Spectroscopy.* Applied Spectroscopy, 1997. **51**(9): p. 1265-1268.
10. Carden, A., et al., *Ultrastructural changes accompanying the mechanical deformation of bone tissue: A Raman imaging study.* Calcified Tissue International, 2003. **72**(2): p. 166-175.
11. Kinoshita, H., et al., *Functional mapping of carious enamel in human teeth with Raman microspectroscopy.* Journal of Raman Spectroscopy, 2008. **39**(5): p. 655-660.
12. Ko, A.C., et al., *Early dental caries detection using a fibre-optic coupled polarization-resolved Raman spectroscopic system.* Optics Express, 2008. **16**(9): p. 6274-6284.
13. Kaminska, K., et al., *Real-time global Raman imaging and optical manipulation of suspended carbon nanotubes.* Physical Review B, 2006. **73**(23).
14. Marcet, S., et al., *Raman spectroscopy hyperspectral imager based on Bragg tunable filters.* Proc. of SPIE, 2012. **8412**: p. 84121J.
15. Gwinnett, A.J., *Structure and composition of enamel.* Operative dentistry, 1992. **Suppl 5**: p. 10-17.
16. Ling, J., et al., *Direct Raman Imaging Techniques for Study of the Subcellular Distribution of a Drug.* Applied Optics, 2002. **41**(28): p. 6006-6017.
17. Šašić, S., *Chemical imaging of pharmaceutical granules by Raman global illumination and near-infrared mapping platforms.* Analytica Chimica Acta, 2008. **611**(1): p. 73-79.
18. McVeigh, P.Z., et al., *Widefield quantitative multiplex surface enhanced Raman scattering imaging in vivo.* J Biomed Opt, 2013. **18**(4): p. 046011.
19. Fincham, A.G., J. Moradian-Oldak, and J.P. Simmer, *The structural biology of the developing dental enamel matrix.* J Struct Biol, 1999. **126**(3): p. 270-99.
20. Nanci, A., *Ten Cate's Oral Histology: Development, Structure, and Function*. 2008: Mosby Elsevier.
21. Song, L., et al., *Photobleaching kinetics of fluorescein in quantitative fluorescence microscopy.* Biophys J, 1995. **68**(6): p. 2588-600.

Figure Captions:

Fig. 1. (a) The schematic diagram of the combined wide-field Raman imaging and Raman spectroscopy system layout. LL: laser line band-pass filter; CL: cylindrical lens; O: low magnification objective; DM: dichroic mirror; EF: edge filter pair; BP: band-pass filter; FBS: flip beam splitter; FL: focusing lens; S: sample. (b) Typical Raman spectra of teeth when the band-pass filter is adjusted to center at 960 cm^{-1} (solid blue curve), 880 cm^{-1} (dashed red curve) and removed (dash-dotted green curve).

Fig. 2. (a) Picture of the sliced cross section of an alligator tooth, the dashed red box showed the area where the wide-field image and the Raman map were acquired. (b) A back-scattered SEM image of the enamel-dentin junction. Wide-field image after narrow band centered at 960 cm^{-1} (c) and 880 cm^{-1}(d) filtration, and the difference of the two images (e). All three wide-field images were normalized by the maximum intensity of image in part c. An f = 25 mm objective

lens was used to focus the laser beam and acquire Raman signal; a negative cylindrical lens (f = −200 mm) was used to expand the laser beam to a line profile. The exposure time was 2 minutes for both parts of b and c. The laser power delivered to the sample was 50 mW. The dashed blue curves indicated the position of the laser beam, which was ellipsoidal in shape.

Fig. 3. (a) Point-by-point Raman map of the alligator tooth. The laser power was 50 mW and the exposure time was 5 s for each spot at 25 μm step size. (b) Fluorescence background corrected wide-field Raman image of Fig. 2e (scale normalized by the maximum intensity in the FOV). The dashed lines show where the transect plots on the sides are generated. (c) Ten points were selected to cover the dental and enamel regions. d) Average values for 960 cm^{-1} Raman intensity of 10 data points in enamel and dentin for point map and global image. The error bars indicate the standard deviation.

Fig. 4. (a) Picture of a human tooth with white lesion, the dashed red box highlights the area where the wide-field image and the Raman maps were acquired. Wide-field image after narrow band centered at 960 cm^{-1} (b) and 880 cm^{-1} (c) background, and the difference of the two images (d). The image in 'c' was normalized by the maximum intensity of image in 'b'. The image in 'd' was presented as the actual CCD values. The acquisition conditions were the same as that reported in Fig. 2.

Fig. 5. (a) Picture of a human tooth with hypomineralized lesion. Point-by-point Raman map of the enamel area (b) and lesion area (c) normalized by the maximum intensity in enamel image shown in the boxes of part a. The laser power was 50 mW and the exposure time was 5 s for

each spot at 25 μm step size. Fluorescence background corrected wide-field Raman image from sound enamel area (d) and lesion (e); the exposure time was 2 minutes and the focal length of the objective lens was 25 mm; no cylindrical lens was inserted. (f) Average 960 cm^{-1} Raman intensity of 10 data points in enamel and lesion parts of point-maps and global images. Error bars indicate the standard deviation. (g) Representative Raman spectra from central enamel and central lesion from hypomineralized lesion, red arrows indicated additional Raman peaks appearing in lesion.

Fig. 6. (a) Picture of a human tooth with hypermineralized lesion. Point-by-point Raman map of the enamel area (b) and lesion area (c) shown in the boxes of part a. The laser power was 50 mW and the exposure time was 5 s for each spot at 25 μm step size. Fluorescence background corrected wide-field Raman image from sound enamel area (d) and lesion area (e); the exposure time was 2 minutes and the focal length of the objective lens was 50 mm; no cylindrical lens was inserted. (f) Representative Raman spectra from central enamel and central lesion from hypermineralized lesion.

Fig. 7. Fluorescence background corrected wide-field Raman images (scale normalized by the maximum intensity in their own FOV) from transition area when f = 25mm (a) and f = 50 (b) objective lens was used; the exposure time was 2 minutes and 4 minutes respectively; the f = −200 mm cylindrical lens was inserted. The dashed red curves indicated the position of the laser beam, which was ellipsoidal in shape.

Fig. 8. Normalized wide-field images of an alligator tooth covering full FOV of the lens before (a) and after (b) the correction of the laser intensity distribution variation by dividing the intensity distribution at full FOV Fig. 2e by the intensity distribution obtained at 880 cm^{-1}. The image in b is normalized with respect to its peak intensity.

Fig. 9. Time-dependent Raman spectra of bovine bone acquired by the 785 nm (upper set) Raman system with 50 mW laser on the sample and 1 s illumination averaged 10 times, and the 1064 nm Raman system (lower set) with 250 mW laser on the sample and 10 s illumination. Black, blue and red spectral profiles indicate 0, 1, and 15 minutes photobleaching.

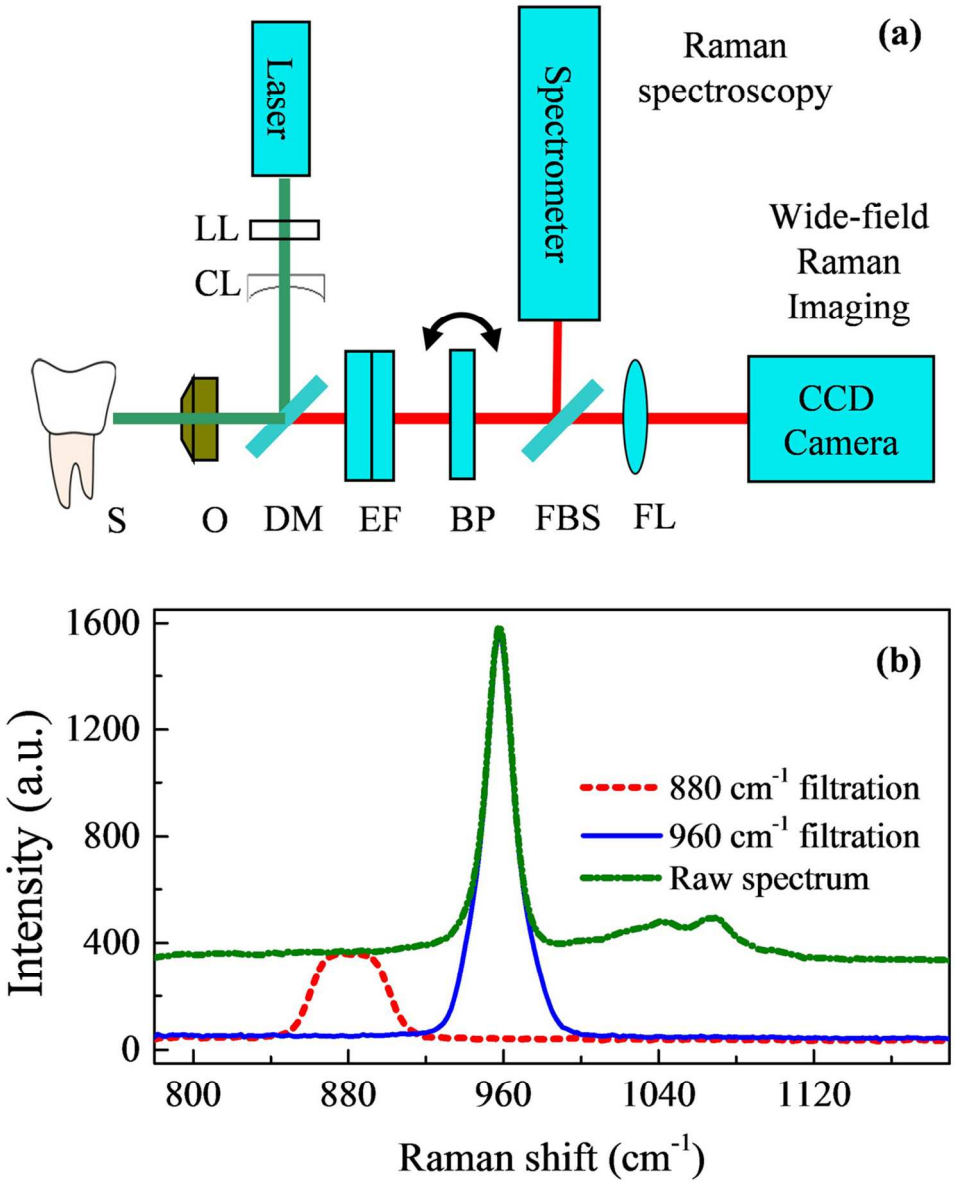

106x131mm (300 x 300 DPI)

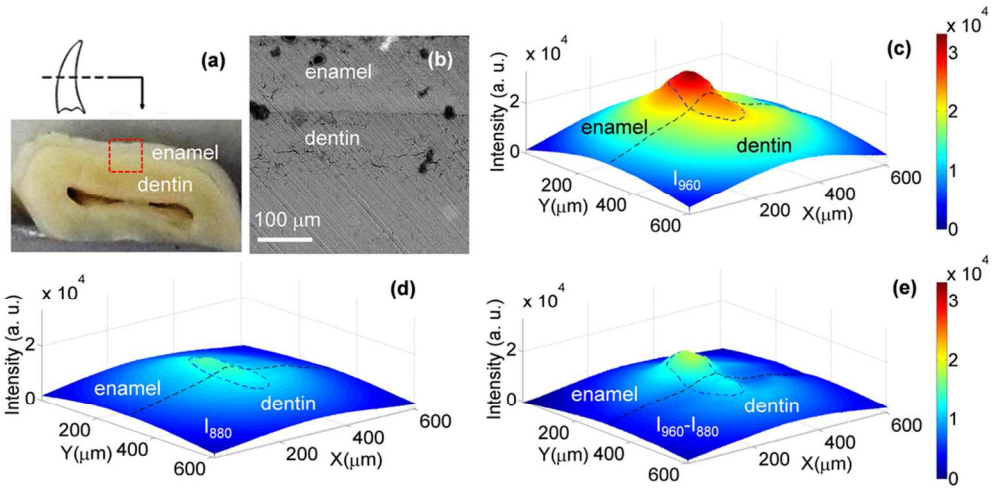

92x48mm (300 x 300 DPI)

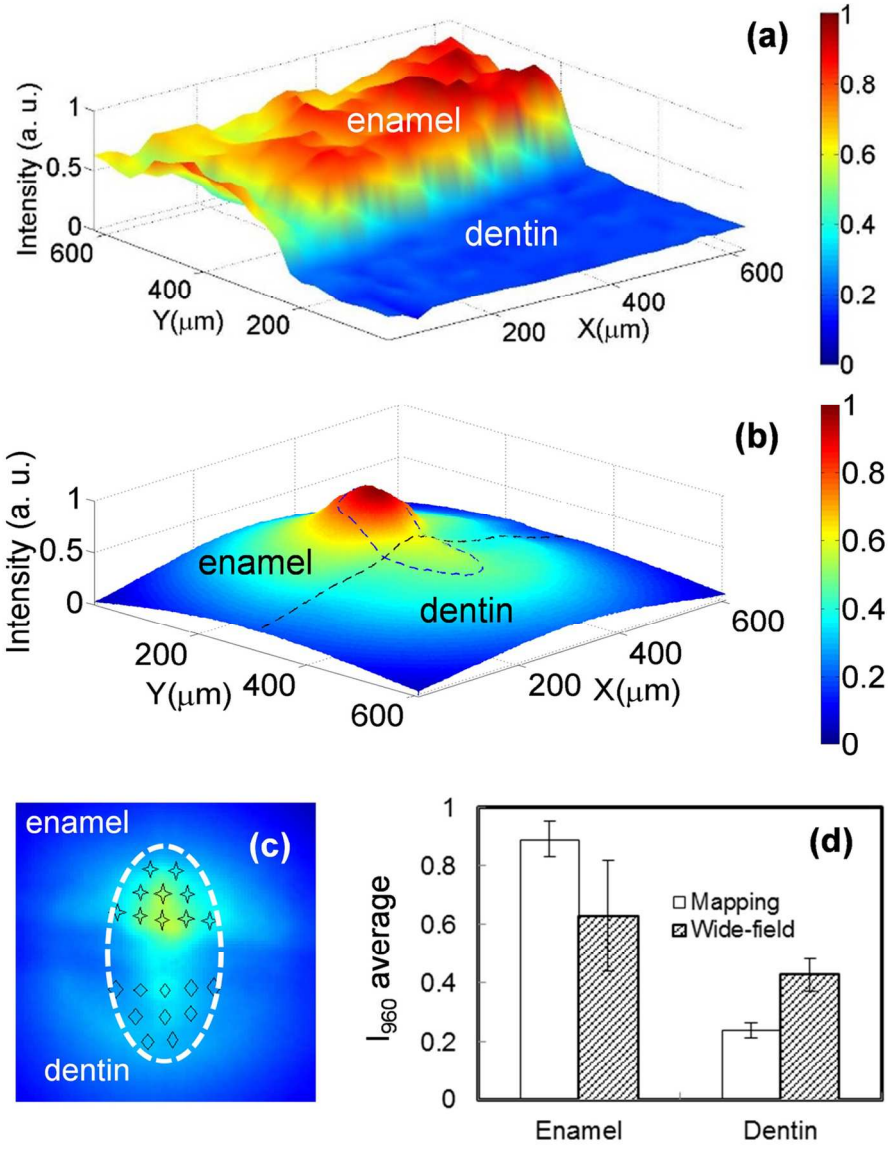

113x148mm (300 x 300 DPI)

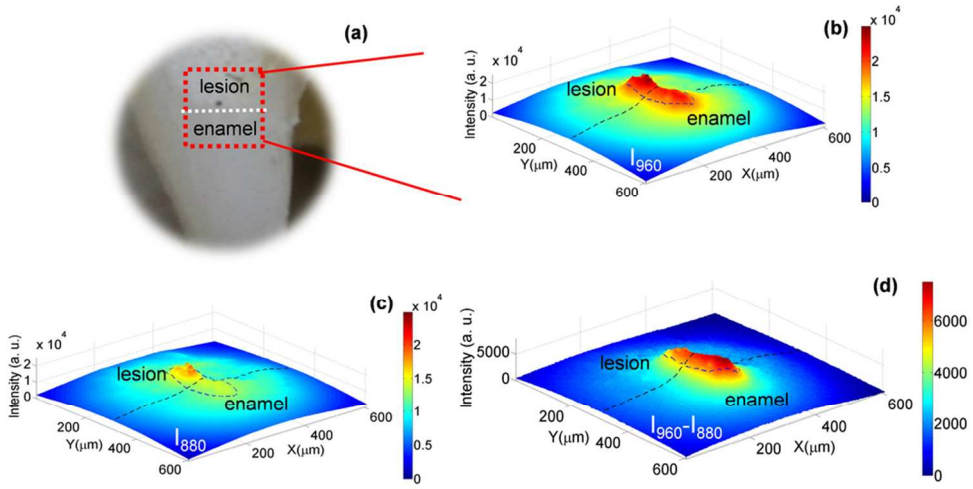

93x49mm (300 x 300 DPI)

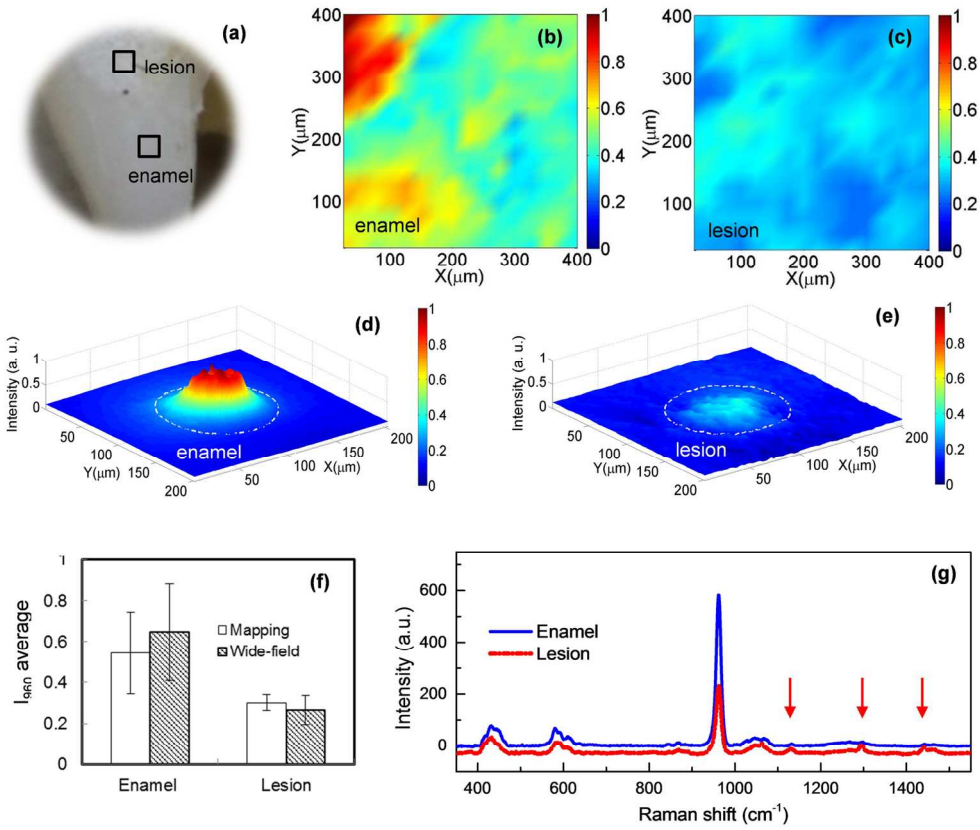

153x132mm (300 x 300 DPI)

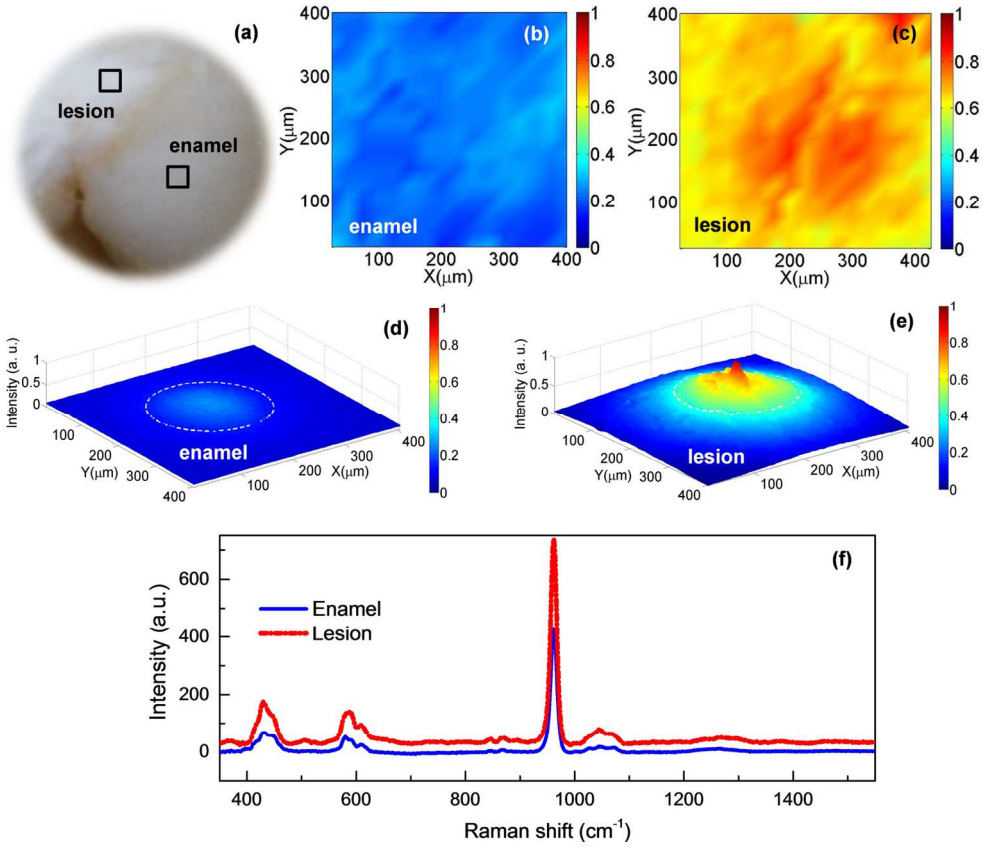

151x128mm (300 x 300 DPI)

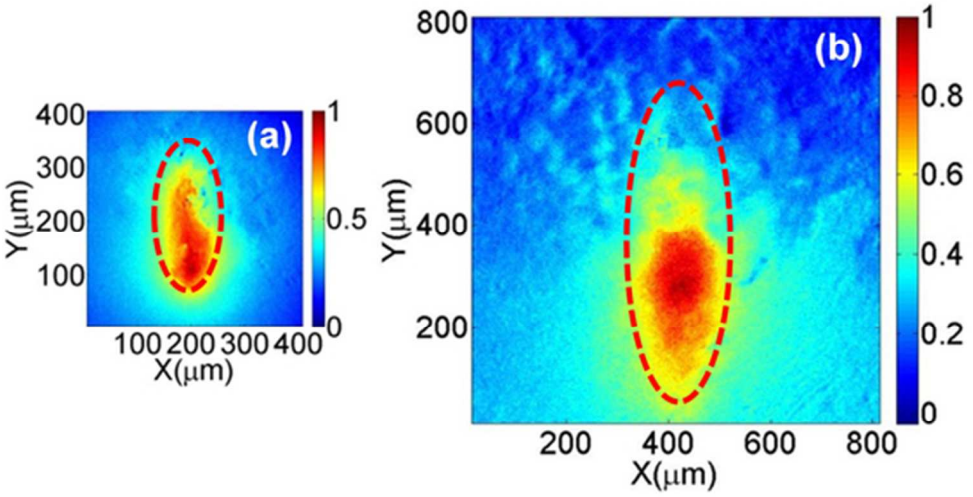

48x27mm (300 x 300 DPI)

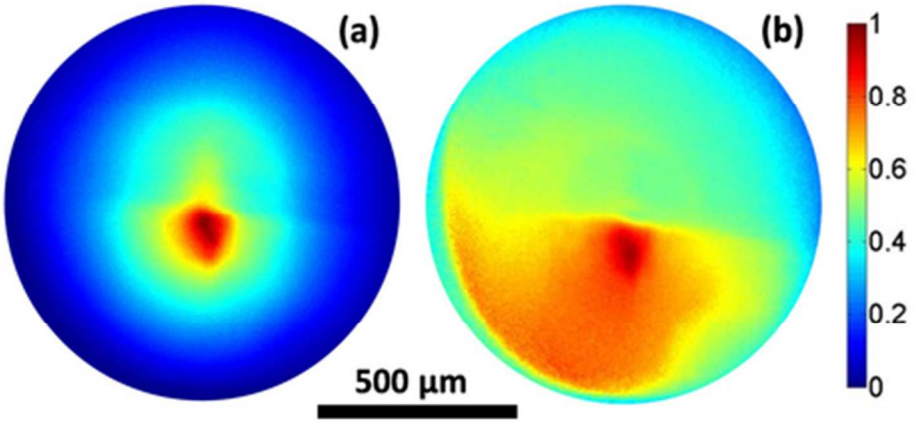

40x18mm (300 x 300 DPI)

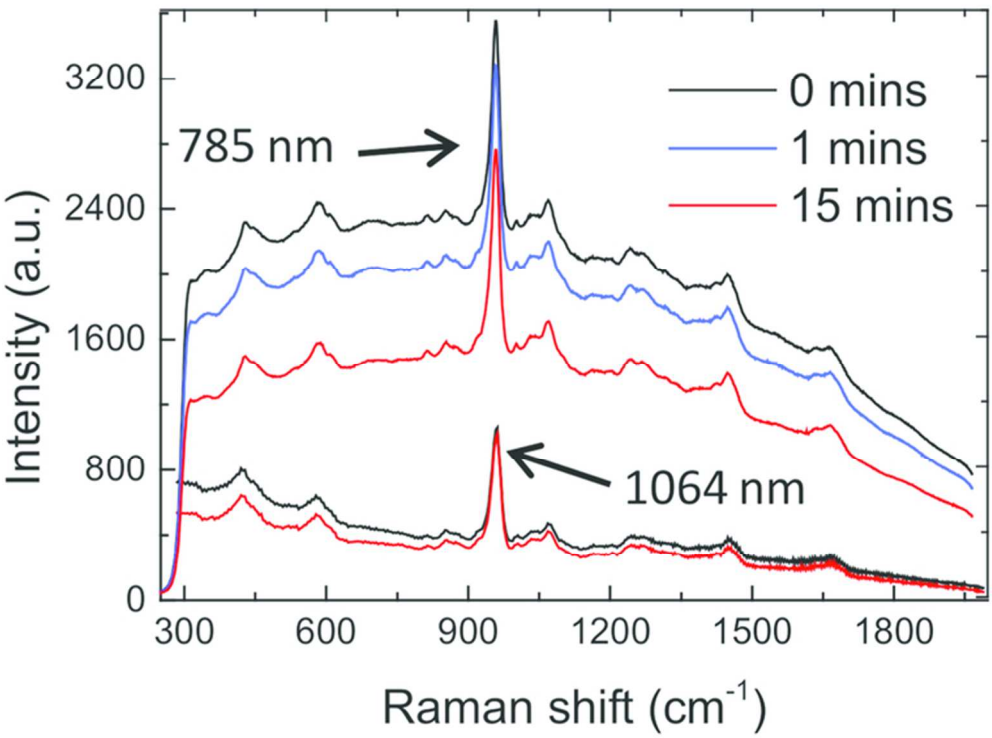

65x49mm (300 x 300 DPI)